

ChartPointFlow for Topology-Aware 3D Point Cloud Generation

Takumi Kimura

Graduate School of System Informatics
Kobe University
Kobe, Japan
kimura@ai.cs.kobe-u.ac.jp

Takashi Matsubara

Graduate School of Engineering Science
Osaka University
Osaka, Japan
matsubara@sys.es.osaka-u.ac.jp

Kuniaki Uehara

Faculty of Business Administration
Osaka Gakuin University
Osaka, Japan
kuniaki.uehara@ogu.ac.jp

Abstract—A point cloud serves as a representation of the surface of a three-dimensional shape. Deep generative models have been adapted to model their variations typically by a map from a ball-like set of latent variables. However, previous approaches have not paid much attention to the topological structure of a point cloud; a continuous map cannot express the varying number of holes and intersections. Moreover, a point cloud is often composed of multiple subparts, and it is also hardly expressed. In this paper, we propose ChartPointFlow, which is a flow-based generative model with multiple latent labels. By maximizing the mutual information, a map conditioned by a label is assigned to a continuous subset of a given point cloud, like a chart of a manifold. This enables our proposed model to preserve the topological structure with clear boundaries, while previous approaches tend to suffer from blurs and to fail in generating holes. Experimental results demonstrate that ChartPointFlow achieves the state-of-the-art performance in generation and reconstruction among sampling-based point cloud generators.

I. INTRODUCTION

A three-dimensional (3D) point cloud, as a set of 3D locations in a Euclidean space, has become a popular representation of a geometric shape [20, 26, 27, 31, 34, 35, 36, 38] (see [8] for a survey). Especially, a point cloud of an object’s surface is easily acquired by sensors such as LiDARs and Kinects. Point clouds can capture a much higher resolution than meshes, and can be processed by simpler manipulations than meshes. By leveraging the flexibility of deep learning, a deep generative model of point clouds enables a variety of synthesis tasks such as generation, reconstruction, and super-resolution [1, 9, 14, 21, 30, 33, 37]. Due to the difficulty in numerically measuring a generated point cloud’s quality, most studies employed flow-based generative models [3, 7, 16] or generative adversarial networks (GANs) [6]. Each method builds a map from a latent object to an object in the data space and evaluates it without a heuristic distance.

As a representation of an object’s surface, a point cloud often has a thin, circular, or hollow structure. Flow-based generative models encounter a difficulty in expressing such manifold-like structure because a bijective map necessary for these models does not exist between a Euclidean space and a manifold with holes, as shown in the top panel of Fig. 1. For expressing a point cloud X lying on the 1-dimensional circle S^1 , a map φ modeled by a neural network squashes a

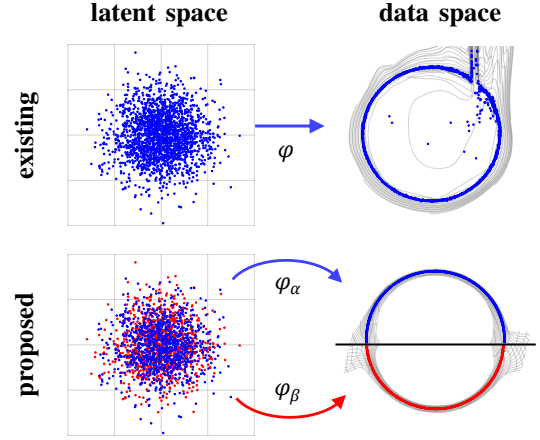


Fig. 1: A conceptual comparison of existing methods (top) and the proposed method (bottom).

2-dimensional ball in a latent space and stretches it to trace an arc, leading to a discontinuity and outliers. Several existing methods have tackled this issue by a flow on a manifold or a dynamic chart method [23, 29]. These methods are, however, applicable only when the geometric property of the target manifold is known and fixed; this assumption does not always hold for point cloud datasets of a variety of shapes. Moreover, a point cloud is often composed of multiple subparts, some of which can be disconnected; it is also hardly expressed. The same goes for GAN-based methods as long as their networks are continuous.

Given the above, we propose *ChartPointFlow*, a generative model for 3D point clouds with latent labels. A map conditioned by a label is assigned to a continuous subset of a given point cloud like a chart of a manifold, and a set of charts forms an atlas that covers the entire point cloud. Taking Fig. 1 as an example, ChartPointFlow with two charts φ_α and φ_β generates two arcs separately and concatenates them in the data space, thereby generating a continuous and hollow circle. For a more complicated object, each chart is assigned to a semantic subpart, e.g., the airframe, right wing, nose, and left wing of an airplane, as shown in Fig. 2. From the viewpoint of the generative model, ChartPointFlow with

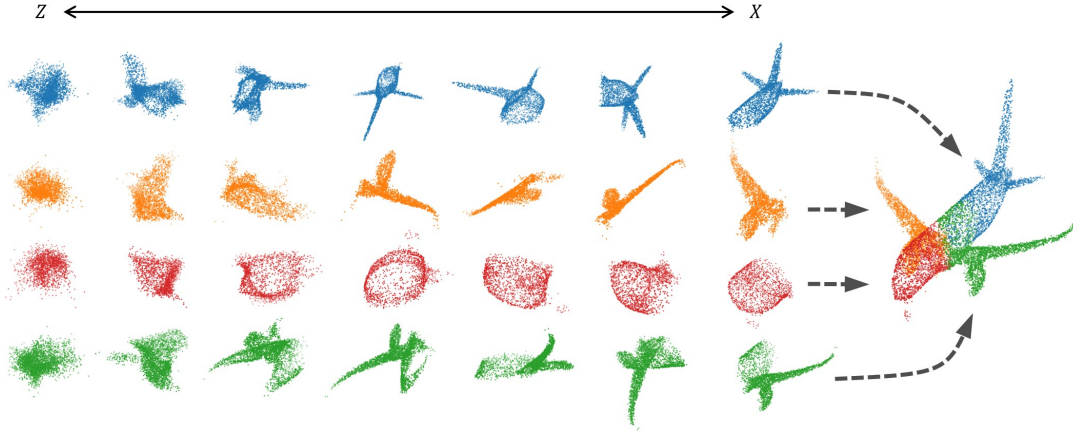


Fig. 2: A visualization of the transformation from a simple distribution in the latent space (left) into a subpart of an object in the data space (right) in the proposed flow-based generative model. Each row corresponds to a chart.

n labels provides a mixture of n distributions.

We evaluate ChartPointFlow on synthetic datasets and ShapeNet datasets [2] of point clouds. Experiments demonstrate that ChartPointFlow preserves the topological structure in detail, while previous approaches tend to generate blurry point clouds and fail in generating holes. Numerical results confirm that ChartPointFlow outperforms the state-of-the-art sampling-based point cloud generators, in particular, r-GAN [1], l-GAN [1], PC-GAN [21], PointFlow [37], and SoftFlow [14].

II. RELATED WORK

Deep Learning on Point Clouds: Since a point cloud is composed of points in no particular order, it requires a specially designed neural network. PointNet took each point separately and performed a permutation-invariant operation (namely, the max-pooling), thereby obtaining the global feature [26]. Following PointNet, many studies have tackled the classification and segmentation tasks [20, 26, 27, 31, 34, 35, 36, 38].

Likelihood-based Point Cloud Generation: One of the earliest models for the point cloud generation is MR-VAE [5], which is based on variational autoencoder (VAE). The VAE is a probabilistic model implemented by two neural networks, namely a decoder that generates a sample and an encoder that performs the variational inference of the latent variable [28]. MR-VAE was trained to minimize a heuristic distance between real and generated point clouds. Zamorski *et al.* [39] employed an adversarial autoencoder to regularize the latent variables.

Yang *et al.* [37] proposed PointFlow as a combination of a permutation-invariant encoder and a point-wise flow-based generative model. A flow-based generative model is a neural network that forms a bijective map and obtains a likelihood by the change-of-variables, and hence it is free from a heuristic distance [3, 7, 16]. Moreover, this architecture can accept and generate an arbitrary number of

points. Because there is no bijective map between manifolds of different topologies, a flow-based generative model tends to be destabilized when modeling zero-width structures like a surface, while this is often the case with the point clouds. Kim *et al.* [14] proposed SoftFlow to address this issue by adding perturbations to points at the training phase.

SoftFlow emphasizes the importance of the topology, but it is still inapplicable to general topological structures, such as holes, intersections, and disconnections. ChartPointFlow tackles this issue.

Likelihood-free Point Cloud Generation: Another group for the point cloud generation is based on GANs. GAN is composed of a pair of neural networks, namely a generator that outputs artificial samples and a discriminator that evaluates their similarity to real samples without a heuristic distance or an explicit likelihood [6]. r-GAN generated all points of a point cloud at once [1]. l-GAN applied a GAN to the feature vector extracted by a pretrained autoencoder [1]. PC-GAN employed a permutation-invariant generator [21], while the above GANs did not.

Other GAN-based approaches can be regarded as a recursive super-resolution. Each model first generates a sparse point cloud, and then it generates more points to interpolate the existing ones, repeatedly [9, 30, 33]. Valsesia *et al.* [33] found that the points close to each other have similar feature vectors. Shu *et al.* [30] also found that each point generated at the first step may be associated with a semantic subpart of the point cloud. These results suggest the importance of the semantic subparts, but these studies never deal with subparts explicitly.

Deep Mixture Generative Model: For modeling samples of multiple categories, deep learning-based generative models have been extended to mixture distributions, such as conditional VAEs [17], conditional GANs [24], and conditional flow-based generative models [3, 16]. The condition is the class label given externally or inferred from data in an unsupervised manner.

ChartPointFlow also infers a label of a sample as a chart that the point belongs to. The main difference is that ChartPointFlow does not assume a mixture distribution. We found that existing generative models encounter a difficulty in expressing even points taken from a single cluster if the cluster has a different topology, as shown in Fig. 1.

III. BACKGROUND

To clarify the issues of existing methods, this section provides preliminary results. We prepared synthetic datasets, namely the circle [7], 2sines [14], and double-moon [3], each of which has only one object X composed of many points $\{x_j\}$, as summarized in Fig. 3. We reduced the noise intensity to make surface-like structures. The top row shows the datasets. The second and third rows show the generation results of PointFlow [37] and SoftFlow [14], where we employed Glow [16] as the backbone. The generated circles and 2sines show the discontinuities and blurred intersections. The generated double-moons show the string-shaped artifacts.

A flow-based generative model is composed of invertible transformations and provides a bijective map between a latent space and a data space (see Appendix A for details on flow-based generative models). As long as the latent space is a Euclidean space, a generated point cloud X is always lying on a connected manifold with no hole. PointFlow and SoftFlow squashed 2-dimensional latent distributions to express thin structures, stretched them to trace arcs, and failed in expressing holes, intersections, and disconnections. The same goes for GAN-based models because a neural network is continuous in general. These results motivate the present study.

IV. FLOW-BASED GENERATIVE MODEL WITH CHARTS

Network Structure: Prior to the proposal of *ChartPointFlow*, we first focus on a generator of a single point cloud X for simplicity. A point generator F is a flow-based generative model of a point $x \in X$ conditioned by a label y . The point generator F conditioned by a label y is regarded as a chart, and a set of n charts form an atlas covering the entire point cloud X . The conditional log-likelihood of the point x is given by the change-of-variables;

$$\log p_F(x|y) = \log p(z) + \log \left| \det \frac{\partial F^{-1}(x;y)}{\partial x} \right|, \quad (1)$$

where z is the latent variable $z = F^{-1}(x;y)$, and its prior $p(z)$ is the standard Gaussian distribution. One can obtain the marginal log-likelihood $\log p_F(x)$ as the sum over all possible labels $\log p_F(x) = \log \sum_y p_F(x|y)p(y)$, but instead, we employed a variational inference model $q_C(y|x)$ implemented as a neural network called a chart predictor C . Then,

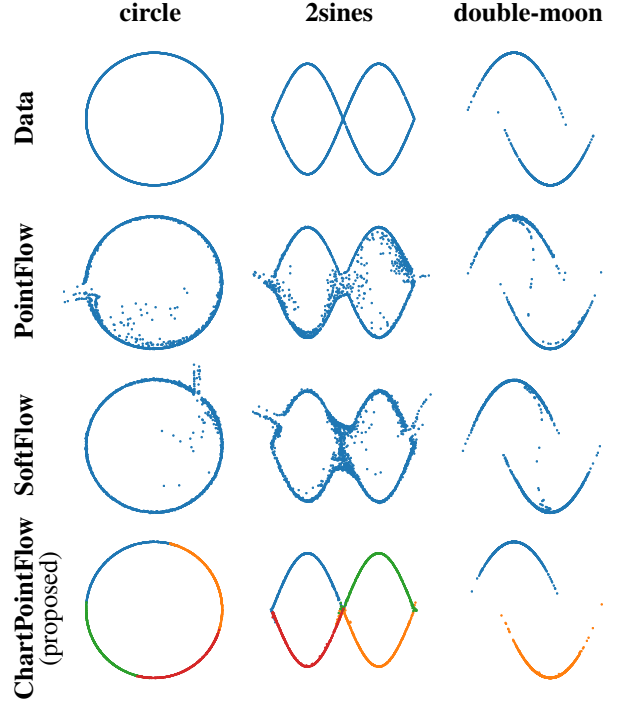


Fig. 3: Point cloud generations by the proposed method, *ChartPointFlow*, with those by PointFlow [37] and SoftFlow [14]. Color represents the chart that the point belongs to.

the negative evidence lower bound (ELBO) $\mathcal{L}_{ELBO}(F; C; x)$ is given by

$$\begin{aligned} \log p_F(x) &= \mathbb{E}_{q_C(y|x)} \left[\log \frac{p_F(x;y) q_C(y|x)}{p_F(y|x) q_C(y|x)} \right] \\ &\geq \mathbb{E}_{q_C(y|x)} \left[\log \frac{p_F(x|y)p(y)}{q_C(y|x)} \right] \\ &= \mathbb{E}_{q_C(y|x)} \left[\log p(z) + \log \left| \det \frac{\partial F^{-1}(x;y)}{\partial x} \right| \right] \\ &\quad - H[q_C(y|x)|p(y)] + H[q_C(y|x)] \\ &\triangleq -\mathcal{L}_{ELBO}(F; C; x), \end{aligned} \quad (2)$$

where $H[q_C(y|x)|p(y)]$ and $H[q_C(y|x)]$ denote the cross-entropy and entropy. We assume that the label prior $p(y)$ is the uniform distribution, and then the cross-entropy $H[q_C(y|x)|p(y)]$ has a constant value; the term is omitted.

Objective Function: The label y is represented by a one-hot vector, and the negative ELBO \mathcal{L} is obtained by the weighted average over all possible labels. This approach requires the computational cost proportional to the number of labels. To surpass it, we employed the Gumbel-Softmax approach [13]. Specifically,

$$\begin{aligned} \tilde{y} &= \text{softmax}((\log \pi_C(x) + \mathbf{g})/\tau) \\ \mathbf{g} &\sim \text{Gumbel}(0, 1), \end{aligned} \quad (3)$$

where \mathbf{g} is a vector each of whose elements follows the Gumbel distribution $\text{Gumbel}(0, 1)$, $\tau \in (0, \infty)$ denotes the temperature of the softmax function, and $\pi_C(x)$ denotes the

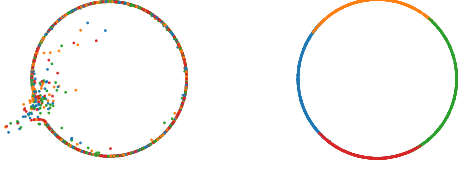


Fig. 4: Contribution of the regularization term \mathcal{L}_{MI} . (left) Result without the regularization term. (right) Result with the regularization term. Color represents the chart that the point belongs to.

vector of the label posterior $q_C(y|x)$, that is, $\pi_C(x)_j = q_C(y_j|x)$. With $\tau \rightarrow +0$, the output \tilde{y} converges to the one-hot vector. With $\tau \rightarrow +\infty$, the output \tilde{y} is the uniform probability vector. This approach allows us the Monte Carlo sampling of the label \tilde{y} in a differentiable form; one can draw an almost one-hot vector \tilde{y} , substitute it into the negative ELBO \mathcal{L} , and train neural networks using gradient descent algorithms. The negative ELBO \mathcal{L} is approximated as

$$\begin{aligned} \mathcal{L}_{ELBO}(F, C; x) \\ \simeq -\log p(z) - \log \left| \det \frac{\partial F^{-1}(x; \tilde{y})}{\partial x} \right| - H[q_C(y|x)] \quad (4) \\ \triangleq \tilde{\mathcal{L}}_{ELBO}(F, C; x), \end{aligned}$$

where the vector \tilde{y} is given by Eq. (3). We emphasize that, thanks to the Gumbel-Softmax approach, the computational cost is constant independently of the number of charts.

When minimizing the approximated negative ELBO $\tilde{\mathcal{L}}$, the entropy $H[q_C(y|x)]$ is maximized, leading to each point belonging to all labels with the same probabilities and the charts overlapped with each other. To assign each chart to a specific connected region of a manifold (that is, a point cloud), we introduce a regularization term $\mathcal{L}_{MI}(x, y)$ based on the mutual information $I(x; y)$;

$$\begin{aligned} -I(y; x) &= -(H[q_C(y)] - H[q_C(y|x)]) \\ &= -H[\mathbb{E}_{p(\tilde{x})}[q_C(y|\tilde{x})]] + H[q_C(y|x)] \\ &\simeq -H\left[\frac{1}{|X|} \sum_{\tilde{x} \in X} q_C(y|\tilde{x})\right] + H[q_C(y|x)] \quad (5) \\ &\triangleq \mathcal{L}_{MI}(C; x). \end{aligned}$$

The minimization of the regularization term \mathcal{L}_{MI} cancels out the maximization of the entropy $H[q_C(y|x)]$ in the negative ELBO $\tilde{\mathcal{L}}(F, C; X)$ and additionally maximizes the entropy $H[q_C(y)]$. Thereby, each sample belongs to only one chart, and all charts are used with uniform probabilities.

For the i.i.d. assumption, the objective function for the entire point cloud X is given by the sum over the points x ;

$$\mathcal{L}(F, C; X, \lambda) = \sum_{x \in X} [\tilde{\mathcal{L}}_{ELBO} + \lambda \mathcal{L}_{MI}], \quad (6)$$

where λ adjusts the regularization term $\mathcal{L}_{MI}(x, y)$.

Experiments on Synthetic Data: We conducted preliminary experiments on 2D synthetic datasets summarized in Fig. 3 to prove the concept of the proposed method. We employed

Glow [16] as the backbone of the point generator F . We used $n = 4$ charts for the circle and 2sines datasets, and $n = 2$ charts for the double-moon dataset. We set λ to 1.05 and τ to 0.1. We trained the models using Adam optimizer [15] with a learning rate of 10^{-4} and a batch size of 100 for 10K iterations. After training, each point x was drawn using the point generator F as

$$x = F(z; y) \text{ for } y \sim p(y) \text{ and } z \sim p(z). \quad (7)$$

We also trained PointFlow [37] and SoftFlow [14] with the same experimental setting. Note that the proposed method without the label is the same as PointFlow.

We summarize the generated point clouds in Fig. 3. PointFlow and SoftFlow generated point clouds suffering from the discontinuities, blurs, artifacts, as mentioned in Section III. In contrast, the proposed model generated a circle without any discontinuity, an intersection free from a severe blur, and two arcs clearly separated without any artifacts. Color represents the chart that the point belongs to. In the circle and 2sines datasets, four subparts are connected smoothly and form the manifold with holes. The intersection is expressed as the intersection of the subparts. In the double-moon dataset, each chart is assigned to one of the arcs exclusively, and thereby expresses the disconnected manifold. These results imply that the proposed concept of the charts works well for various topological structures even with the same latent variable distribution $p(z)$.

To evaluate the regularization term \mathcal{L}_{MI} , we also set the coefficient λ to 0 and summarize the results in Fig. 4. Without the regularization term \mathcal{L}_{MI} , each label is assigned to the entire point cloud overlapped with each other, and the model generated the discontinuity. This is because the maximization of the entropy $H[q_C(y|x)]$ leads to the uniform posterior $q_C(y|x)$, and each label works similarly.

V. CHARTPOINTFLOW

In this section, we extend the model proposed in Section IV for applying it to 3D point cloud datasets, and name it *ChartPointFlow*. Figure 5 shows the conceptual diagram. We assume that a point cloud dataset \mathcal{X} is composed of N objects $\{X_1, X_2, \dots, X_N\}$, and each object X_i is represented by a cloud of M_i points $\{x_1, x_2, \dots, x_{M_i}\}$.

Network Structure: In ChartPointFlow, a permutation-invariant neural network called a feature encoder E accepts a point cloud X consisting of M points and encodes it to a posterior $q_E(s_X|X)$ of a feature vector s_X using the reparameterization trick [19]. The feature vector s_X is considered as a representation of the entire shape of the point cloud X . With a Gaussian prior, the reparameterization trick is known to suffer from the posterior collapse, where the output s_X ignores the input X [18, 37]. To make the prior more expressive, we employ a flow-based generative model called a prior flow G , which maps the feature vector s_X to the latent

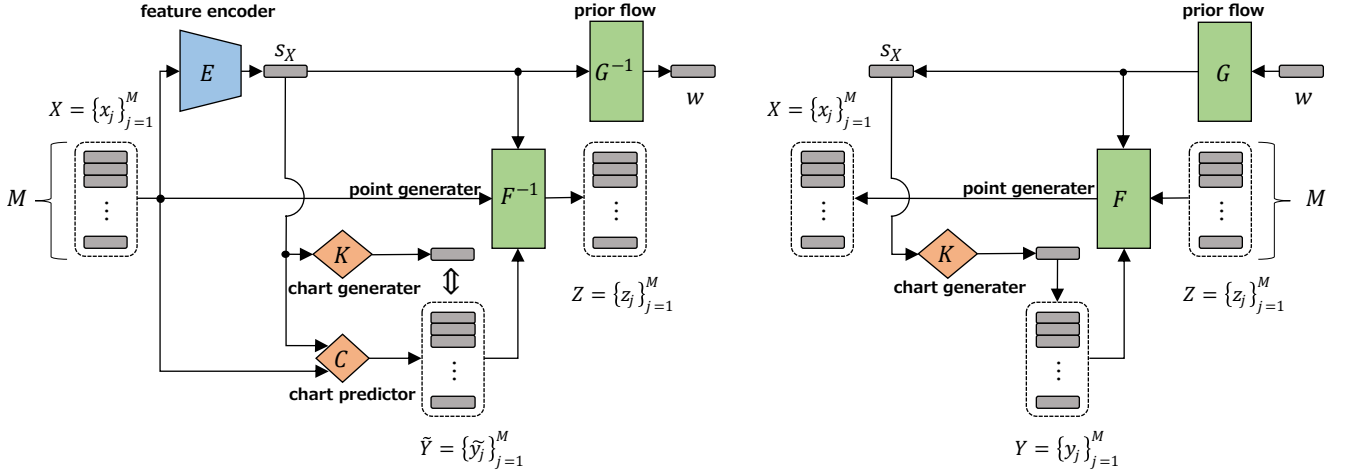


Fig. 5: Architectures and data flow at the training phase (left) and at the generation phase (right).

variable w . Then, the trainable prior $p_G(s_X)$ of the feature vector s_X is given by

$$\log p_G(s_X) = \log p(w) + \int_{t_0}^{t_1} \log \left| \det \frac{\partial G^{-1}(s_X)}{\partial s_X} \right|. \quad (8)$$

where $w = G^{-1}(s_X)$ and the prior $p(w)$ is set to the standard Gaussian distribution. Thereby, the prior flow G learns the distribution of point clouds.

As a part of ChartPointFlow, the chart predictor $q_C(y|x, s_X)$ is conditioned by the feature vector s_X ; it accepts a point $x \in X$ and infers the label y that corresponds to the chart that the point x belongs to. The condition by s_X implies that different point clouds have different atlases even in the same dataset; for example, points in the same location can be a part of an engine or the airframe depending on the airplane's width.

The point generator F is also conditioned by the feature vector s_X as well as the label y to generate different shapes. Then, the log-likelihood of a point x is given by

$$\log p_F(x|y, s_X) = \log p(z) + \log \left| \det \frac{\partial F^{-1}(x; y, s_X)}{\partial x} \right|. \quad (9)$$

Despite the uniform prior $p(y)$ of the label y , the size of a subpart can depend on point clouds X , and the posterior of the label y is $q_C(y|X, s_X) = \mathbb{E}_{x \in X} \sum_j q_C(y|x, s_X)$. For the generation task, we further introduce a neural network named the chart generator K , which accepts a feature vector s_X and gives the posterior $p_K(y|s_X)$ of the label y .

Objective Function: Let Y denote a set of labels, each of which corresponds to a point x of the given point cloud X . Due to the i.i.d. assumption, $p(Y) = \prod_j p(y_j)$, $q_C(Y|s_X) = \prod_j q_C(y_j|s_X)$, and $p_F(X|Y, s_X) = \prod_j p_F(x_j|y_j, s_X)$. Given

the above, the negative ELBO \mathcal{L}_{ELBO} is given by

$$\begin{aligned} & \log p(X) \\ & \geq \mathbb{E}_{q_E(s_X|X)} q_C(Y|X, s_X) \left[\log \frac{p_F(X|Y, s_X) p(Y) p_G(s_X)}{q_C(Y|X, s_X) q_E(s_X|X)} \right] \\ & = \mathbb{E}_{q_E(s_X|X)} \left[\sum_j \left\{ \mathbb{E}_{q_C(y_j|x_j, s_X)} [\log p_F(x_j|y_j, s_X)] \right. \right. \\ & \quad \left. \left. - H(q_C(y_j|x_j, s_X)) \right\} \right] - H[q_E(s_X|X) | p_G(s_X)] \\ & \triangleq -\mathcal{L}_{ELBO}(F, C, E, G; X). \end{aligned} \quad (10)$$

In practice, the expectation $\mathbb{E}_{q_C(y_j|x_j, s_X)}$ over the label y_j is approximated by the Gumbel-Softmax [13] (see Eq. (3)), and the expectation $\mathbb{E}_{q_E(s_X|X)}$ over the feature vector s_X is approximated by Monte Carlo sampling [19]. The approximated negative ELBO is denoted by $\tilde{\mathcal{L}}_{ELBO}(F, C, E, G; X)$.

While the first term of the regularization term in Eq. (5) forces each object to use all charts equivalently, each chart may have its own size in practice. For a flexible adjustment, we introduce coefficient terms μ and λ as

$$\sum_j \left\{ -\mu H \left[\frac{1}{|X|} \sum_{\tilde{x} \in X} q_C(y_j|\tilde{x}) \right] + \lambda H[q_C(y_j|x_j)] \right\} \triangleq \mathcal{L}_{MI}(C; X, \mu, \lambda). \quad (11)$$

Then, the objective function is

$$\mathcal{L}(F, C, E, G, K; \mathcal{X}, \mu, \lambda) = \sum_{X \in \mathcal{X}} \left[\tilde{\mathcal{L}}_{ELBO} + \mathcal{L}_{MI} \right]. \quad (12)$$

In addition, the chart generator K is separately trained to estimate the label posterior $q_C(y|X)$ by minimizing the objective function

$$\mathcal{L}_{CP}(K; X) = D_{KL}(p_K(y|s_X) \| q_C(y|X)). \quad (13)$$

Usage and Tasks: For the generation tasks, one can follow the right panel of Fig. 5. One first draws a latent variable w from the prior $p(w)$ and feeds it to the prior flow G , obtaining a feature vector $s_X = G(w)$. Feeding the feature

vector s_X to the chart generator K , one gets the posterior $p_K(y|s_X)$ of the label y as a categorical distribution. One repeats the following step M times for M points: one draws a label y_j from the posterior $p_K(y|s_X)$ and a latent variable z_j from the prior $p(z_j)$, feeds them to the point generator F , and obtains a point $x_j = F(z_j; y_j, s_X)$. Then, the set of the obtained points is the generated point cloud X . Formally, $p(X) = \int_{s_X} p_G(s_X) \prod_j \int_{y_j} p_F(x_j|y_j, s_X) p_K(y_j|s_X)$.

For the reconstruction or super-resolution tasks, one feeds a given point cloud X to the feature encoder E and obtains a feature vector s_X instead of drawing the feature vector s_X from the prior flow G . Drawing the same number of points is called reconstruction, and drawing more points is called super-resolution.

The computational cost of ChartPointFlow is almost the same as those of the comparative methods PointFlow [37] and SoftFlow [14]. Recall that the computational cost of the proposed method is constant independently of the number of charts thanks to the Gumbel-Softmax approach. The chart predictor C is used only at the training phase. The computational cost of the chart generator K is negligible because it is proportional to the number of point clouds (i.e., objects) while other components E , F , and C require a computational cost proportional to the number of points in all point clouds.

VI. EXPERIMENTS AND RESULTS

A. Experimental Settings

We evaluate ChartPointFlow using the ShapeNet dataset [2]. ShapeNet is composed of 513,000 unique 3D objects of 55 categories. From the categories, we took three different categories; airplane, chair, and car, following Yang *et al.* [37].

We followed the experimental settings of SoftFlow’s release code [14]. We trained 15K epoch in each category using Adam optimizer [15] with a batch size of 128, a initial learning rate of 2.0×10^{-3} , $\beta_1 = 0.9$, and $\beta_2 = 0.999$. We decayed the learning rate by quarter after every 5K epoch. We obtained $M = 2,048$ points randomly from each object X . For the reconstruction task, we obtained another set of 2,048 points per object for evaluation.

We set $\tau = 0.1$ for the Gumbel-Softmax approach, set $\mu = 0.05$ and $\lambda = 1.0$ for the regularization term \mathcal{L}_{MI} , and searched the number n of charts from a range of $\{4, 8, 12, 16, 20, 24\}$. The architectures and sizes of neural networks followed those of PointFlow [37] and SoftFlow [14]. The details are summarized in Appendix B.

B. Evaluation Metrics

For measuring a distance between a pair of point clouds X_1 and X_2 , permutation-invariant metrics, Chamfer distance

(CD) and earth mover’s distance (EMD) have been commonly used [1, 14, 21, 37]. They are given by

$$\begin{aligned} CD(X_1, X_2) &= \sum_{x \in X_1} \min_{\xi \in X_2} \|x - \xi\|_2^2 + \sum_{x \in X_2} \min_{\xi \in X_1} \|x - \xi\|_2^2, \\ EMD(X_1, X_2) &= \min_{\phi: X_1 \rightarrow X_2} \sum_{x \in X_1} \|x - \phi(x)\|_2, \end{aligned} \quad (14)$$

where both point clouds X_1 and X_2 are composed of the same number of points, ϕ is a bijective map from the point cloud X_1 to the other X_2 , and $\|\cdot\|_2$ denotes the Euclidean distance on \mathbb{R}^3 .

For evaluating the similarity between a pair of sets \mathcal{X}_1 and \mathcal{X}_2 of point clouds, previous studies have proposed several metrics, namely Jensen-Shannon divergence (JSD), minimum matching distance (MMD), coverage (COV), and 1-nearest neighbor accuracy (1-NNA) [1, 14, 21, 22, 37]. However, recent studies have revealed that JSD, MMD, and COV may give good scores to poor models [14, 37]. For example, JSD gives a good score to a model that generates an average shape without considering individual shapes [37]. Here, we evaluated models with 1-NNA; the results with other metrics are summarized in Appendix C1 just for reference.

1-NNA aim to evaluate whether two distributions are identical for two-sample tests. The definition is

$$\begin{aligned} 1\text{-NNA}(\mathcal{X}_1, \mathcal{X}_2) &= \frac{\sum_{X_1 \in \mathcal{X}_1} \mathbb{1}[N_{X_1} \in \mathcal{X}_1] + \sum_{X_2 \in \mathcal{X}_2} \mathbb{1}[N_{X_2} \in \mathcal{X}_2]}{|\mathcal{X}_1| + |\mathcal{X}_2|}, \end{aligned} \quad (15)$$

where both sets \mathcal{X}_1 and \mathcal{X}_2 are composed of the same number of point clouds, N_{X_\bullet} gives the nearest neighbor of X_\bullet in $\mathcal{X}_1 \cup \mathcal{X}_2 - \{X_\bullet\}$, and $\mathbb{1}[\cdot]$ is the indicator function. Roughly speaking, a 1-nearest neighbor classifier classifies a given point cloud X into \mathcal{X}_1 or \mathcal{X}_2 according to the nearest sample N_X in terms of the CD or EMD. The closer to 50% the accuracy of 1-NNA is, the more similar the distributions \mathcal{X}_1 and \mathcal{X}_2 are.

C. Generation Task

For the generation task, we compared ChartPointFlow with comparative sampling-based generators, namely r-GAN [1], l-GAN [1], PC-GAN [21], PointFlow [37], and SoftFlow [14], for a fair comparison. The results of the comparative methods were obtained from [37] and [14].

We took the average over 16 runs to surpass the variance due to the randomness in the generation. The results are summarized in Table I. The top four methods are based on GANs, and the others are flow-based generative models. One can see that ChartPointFlow outperforms the others in all categories. We provided the results of ChartPointFlow with 24, 20, and 16 charts for the airplane, chair, and car categories, respectively, but the performances were consistent over 12–24 charts; the results with different numbers of charts are summarized in Appendix C2.

Figure 6 shows the samples generated by ChartPointFlow, each of which is composed of 10,000 points. Each of an object’s protruding subparts such as the airplane’s horizontal

Category	Model	CD	EMD
Airplane	r-GAN [1]	93.58	99.51
	l-GAN (CD) [1]	86.30	97.28
	l-GAN (EMD) [1]	87.65	85.68
	PC-GAN [21]	94.35	92.32
	PointFlow [37]	75.68	75.06
	SoftFlow [14]	70.92	69.44
	ChartPointFlow	69.39	65.62
Chair	r-GAN [1]	71.75	99.47
	l-GAN (CD) [1]	64.43	85.27
	l-GAN (EMD) [1]	64.73	65.56
	PC-GAN [21]	76.03	78.37
	PointFlow [37]	60.88	59.89
	SoftFlow [14]	59.95	63.51
	ChartPointFlow	57.89	58.31
Car	r-GAN [1]	97.87	99.86
	l-GAN (CD) [1]	63.07	88.07
	l-GAN (EMD) [1]	69.74	68.32
	PC-GAN [21]	92.19	90.87
	PointFlow [37]	60.65	62.36
	SoftFlow [14]	62.63	64.71
	ChartPointFlow	58.13	58.80

TABLE I: Generation results evaluated by 1-NNA. A score closer to 50% is better.

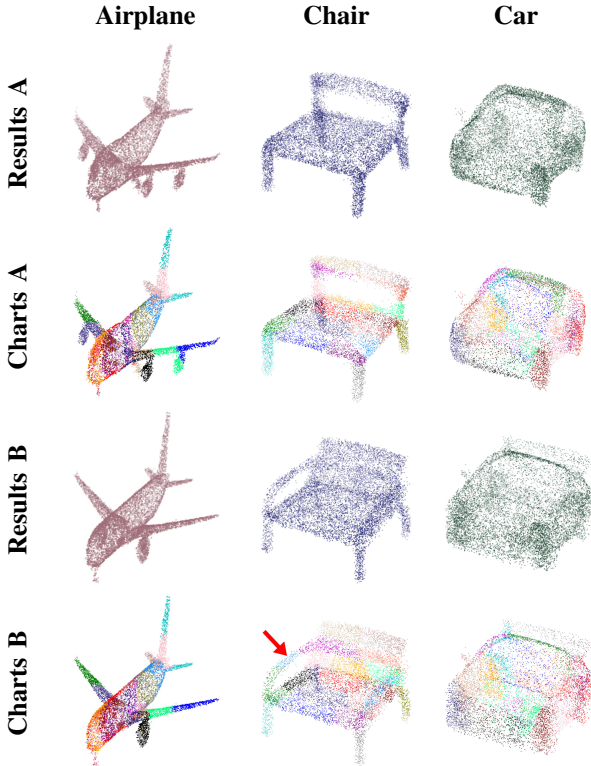


Fig. 6: Generation examples by ChartPointFlow.

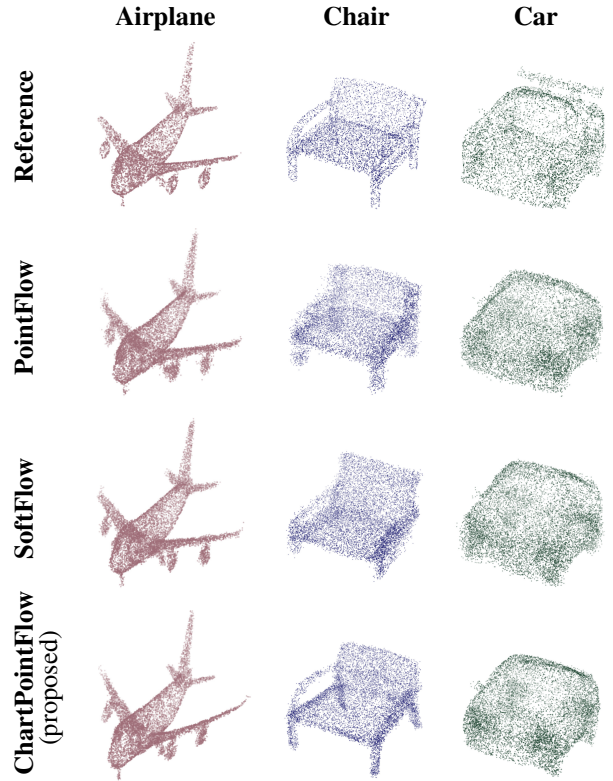


Fig. 7: Generation examples nearest to the references taken from the datasets.

tails, the chair’s legs, and the cars’ wheels is expressed by its own chart. The same subparts are expressed by the same charts across the objects. The chair in the top panel does not have armrests and does not use the charts assigned to the armrests of the chair in the bottom panel (see the red arrow). The same goes for the cars’ rear spoiler. ChartPointFlow assigned several charts to the chair’s seat and armrests only when needed, and thereby expressed the varying topologies. Other results are summarized in Appendix C3

For comparison, we took reference samples from the evaluation subsets and chose the nearest samples in terms of EMD from the samples generated by each model, as shown in Fig. 7. We employed pretrained models of PointFlow¹ and SoftFlow² distributed by the authors. ChartPointFlow generated the nearer samples than others, suggesting that ChartPointFlow generated a variety of shapes.

D. Reconstruction Task

For the reconstruction task, we measured the distance (CD and EMD) between a reference point cloud and a reconstructed one, and summarized the results averaged over five trials in Table II. In this section, we used the pretrained model of PointFlow trained only in the reconstruction task, while ChartPointFlow and SoftFlow were trained only in the generation task.

¹<https://github.com/stevenygd/PointFlow>

²<https://github.com/ANLGBOY/SoftFlow>

Category	Model	CD	EMD
Airplane	PointFlow	1.21	2.77
	SoftFlow	1.19	2.60
	ChartPointFlow	1.07	2.23
Chair	PointFlow	10.09	6.42
	SoftFlow	11.04	6.60
	ChartPointFlow	8.78	4.62
Car	PointFlow	6.54	5.16
	SoftFlow	6.82	5.08
	ChartPointFlow	6.20	3.96

TABLE II: Reconstruction performances evaluated by CD ($\times 10^4$) and EMD ($\times 10^2$).

ChartPointFlow with 24 charts outperforms the comparative methods in all categories. The improvement is the most significant for the chair. This may be because the chair dataset shows the varying shape of legs and the varying number of holes in the backrest, in short, the varying topologies. Figure 8 shows that ChartPointFlow reconstructed such shapes clearly. Moreover, ChartPointFlow reconstructed even the airplane’s front wheel and the car’s mirrors. PointFlow and SoftFlow tried to reconstruct a variety of shapes from one latent variable set and failed in generating the holes under the chair’s backrest and armrests. See Appendices C2 and C3 for more results.

VII. CONCLUSION

This paper proposed ChartPointFlow, which is a flow-based generative model of point clouds employing multiple charts. With an appropriate regularization, each chart is assigned to a semantic subpart of a point cloud, thereby expressing a variety of shapes with different topologies. Thanks to the Monte Carlo sampling, the computational cost is of the same order as the case without charts. The performance was evaluated using three 2D synthetic datasets and three 3D practical datasets, and the results demonstrated that ChartPointFlow generates various point clouds of various shapes with accuracies much better than comparative methods. The main concept of the charts is not limited to flow-based generative models; future work includes the application to other methods, such as a recursive super-resolution [9, 30, 33].

REFERENCES

- [1] Panos Achlioptas, Olga Diamanti, Ioannis Mitliagkas, and Leonidas Guibas. Learning representations and generative models for 3d point clouds. In *International Conference on Machine Learning (ICML)*, 2018. 1, 2, 6, 7, 10, 11
- [2] Angel X. Chang, Thomas Funkhouser, Leonidas Guibas, Pat Hanrahan, Qixing Huang, Zimo Li, Silvio Savarese, Manolis Savva, Shuran Song, Hao Su, Jianxiong Xiao, Li Yi, and Fisher Yu. ShapeNet: An information-rich 3d model repository. *arXiv preprint arXiv:1512.03012*, 2015. 2, 6
- [3] Laurent Dinh, Jascha Sohl-Dickstein, and Samy Bengio. Density estimation using real NVP. In *International Conference on Learning Representations (ICLR)*, 2017. 1, 2, 3, 9

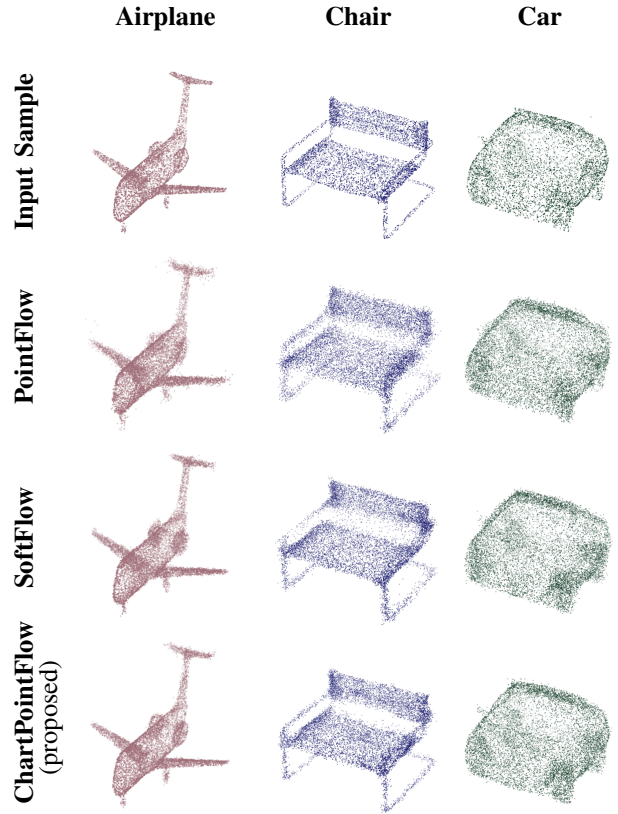


Fig. 8: Reconstruction examples.

- [4] Harrison Edwards and Amos Storkey. Towards a Neural Statistician. In *International Conference on Learning Representations (ICLR)*, 2016. 10
- [5] Matheus Gadelha, Rui Wang, and Subhansu Maji. Multiresolution tree networks for 3d point cloud processing. In *European Conference on Computer Vision (ECCV)*, 2018. 2
- [6] Ian J Goodfellow, Jean Pouget-abadie, Mehdi Mirza, Bing Xu, and David Warde-farley. Generative Adversarial Nets. In *Advances in Neural Information Processing Systems (NIPS)*, 2014. 1, 2
- [7] Will Grathwohl, Ricky T. Q. Chen, Jesse Bettencourt, Ilya Sutskever, and David Duvenaud. Ffjord: Free-form continuous dynamics for scalable reversible generative models. In *International Conference on Learning Representations (ICLR)*, 2019. 1, 2, 3, 9, 10
- [8] Yulan Guo, Hanyun Wang, Qingyong Hu, Hao Liu, Li Liu, and Mohammed Bennamoun. Deep learning for 3D point clouds: A survey. *IEEE Transactions on Pattern Analysis and Machine Intelligence*, 2019. 1
- [9] Le Hui, Rui Xu, Jin Xie, Jianjun Qian, and Jian Yang. Progressive Point Cloud Deconvolution Generation Network. In *European Conference on Computer Vision (ECCV)*, 2020. 1, 2, 8
- [10] M.F. Hutchinson. A stochastic estimator of the trace of the influence matrix for laplacian smoothing splines. *Communications in Statistics - Simulation and Computation*, 18:1059–1076, 1989. 10
- [11] Sergey Ioffe and Christian Szegedy. Batch Normalization: Accelerating Deep Network Training by Reducing Internal Covariate Shift. In *International Conference on Machine Learning (ICML)*, 2015. 10
- [12] Jörn-Henrik Jacobsen, Arnold Smeulders, and Edouard Oyallon. i-RevNet: Deep Invertible Networks. In *International Conference on Learning Representations (ICLR)*, 2018. 9
- [13] Eric Jang, Shixiang Gu, and Ben Poole. Categorical reparameterization with gumbel-softmax. In *International Conference on Learning Representations (ICLR)*, 2017. 3, 5, 10
- [14] Hyeonju Kim, Hyeonseung Lee, Woo Hyun Kang, Joun Yeop Lee, and Nam Soo Kim. SoftFlow: Probabilistic Framework for Normalizing Flow on Manifolds. *arXiv preprint arXiv:2006.04604*, 2020. 1, 2, 3, 4, 6, 7, 10, 11

- [15] Diederik P. Kingma and Jimmy Ba. Adam: A Method for Stochastic Optimization. In *International Conference on Learning Representations (ICLR)*, 2015. 4, 6
- [16] Diederik P. Kingma and Prafulla Dhariwal. Glow: Generative flow with invertible 1x1 convolutions. In *Advances in Neural Information Processing Systems (NeurIPS)*, 2018. 1, 2, 3, 4, 9, 10
- [17] Diederik P. Kingma, Danilo J. Rezende, and Max Welling. Semi-supervised Learning with Deep Generative Models. In *Advances in Neural Information Processing Systems (NIPS)*, 2014. 2
- [18] Diederik P. Kingma, Tim Salimans, Rafal Jozefowicz, Xi Chen, Ilya Sutskever, and Max Welling. Improved variational inference with inverse autoregressive flow. In *Advances in Neural Information Processing Systems (NIPS)*, 2016. 4, 9
- [19] Diederik P. Kingma and Max Welling. Auto-encoding variational bayes. In *International Conference on Learning Representations (ICLR)*, 2014. 4, 5
- [20] Roman Kulkov and Victor Lempitsky. Escape from Cells: Deep Kd-Networks for the Recognition of 3D Point Cloud Models. In *International Conference on Computer Vision (ICCV)*, 2017. 1, 2
- [21] Chun Liang Li, Manzil Zaheer, Yang Zhang, Barnabás Póczos, and Ruslan Salakhutdinov. Point cloud gan. In *Deep Generative Models for Highly Structured Data, International Conference on Learning Representations (ICLR) Workshop*, 2019. 1, 2, 6, 7, 10, 11
- [22] David Lopez-Paz and Maxime Oquab. Revisiting classifier two-sample tests. In *International Conference on Learning Representations (ICLR)*, 2017. 6, 10
- [23] Aaron Lou, Derek Lim, Isay Katsman, Leo Huang, Qingxuan Jiang, Ser-Nam Lim, and Christopher De Sa. Neural Manifold Ordinary Differential Equations. In *Advances in Neural Information Processing Systems (NeurIPS)*, 2020. 1
- [24] Mehdi Mirza and Simon Osindero. Conditional Generative Adversarial Nets. *arXiv preprint arXiv:1411.1784*, 2014. 2
- [25] George Papamakarios, Theo Pavlakou, and Iain Murray. Masked Autoregressive Flow for Density Estimation. In *Advances in Neural Information Processing Systems (NIPS)*, 2017. 9
- [26] Charles R. Qi, Hao Su, Kaichun Mo, and Leonidas J. Guibas. PointNet: Deep learning on point sets for 3D classification and segmentation. In *Computer Vision and Pattern Recognition (CVPR)*, 2017. 1, 2
- [27] Charles R. Qi, Li Yi, Hao Su, and Leonidas J. Guibas. PointNet++: Deep hierarchical feature learning on point sets in a metric space. In *Advances in Neural Information Processing Systems (NeurIPS)*, 2017. 1, 2
- [28] Danilo Jimenez Rezende and Shakir Mohamed. Variational inference with normalizing flows. In *International Conference on Machine Learning (ICML)*, 2015. 2
- [29] Danilo Jimenez Rezende, George Papamakarios, Sébastien Racanière, Michael S. Albergo, Gurtej Kanwar, Phiala E. Shanahan, and Kyle Cranmer. Normalizing Flows on Torii and Spheres. In *International Conference on Machine Learning (ICML)*, 2020. 1
- [30] Dongwook Shu, Sung Woo Park, and Junseok Kwon. 3D point cloud generative adversarial network based on tree structured graph convolutions. In *International Conference on Computer Vision (ICCV)*, 2019. 1, 2, 8
- [31] Hang Su, Varun Jampani, Deqing Sun, Subhansu Maji, Evangelos Kalogerakis, Ming Hsuan Yang, and Jan Kautz. SPLATNet: Sparse Lattice Networks for Point Cloud Processing. In *Computer Vision and Pattern Recognition (CVPR)*, 2018. 1, 2
- [32] Takeshi Teshima, Isao Ishikawa, Koichi Tojo, Kenta Oono, Masahiro Ikeda, and Masashi Sugiyama. Coupling-based Invertible Neural Networks Are Universal Diffeomorphism Approximators. In *Advances in Neural Information Processing Systems (NeurIPS)*, 2020. 9
- [33] Diego Valsesia, Giulia Fracastoro, and Enrico Magli. Learning localized generative models for 3D point clouds via graph convolution. In *International Conference on Learning Representations (ICLR)*, 2019. 1, 2, 8
- [34] Lei Wang, Yuchun Huang, Yaolin Hou, Shenman Zhang, and Jie Shan. Graph Attention Convolution for Point Cloud Semantic Segmentation. In *Computer Vision and Pattern Recognition (CVPR)*, 2019. 1, 2
- [35] Panqu Wang and Ulrich Neumann. Grid-GCN for Fast and Scalable Point Cloud Learning. In *Computer Vision and Pattern Recognition (CVPR)*, 2020. 1, 2
- [36] Xu Yan, Chaoda Zheng, Zhen Li, Sheng Wang, and Shuguang Cui. PointASNL: Robust Point Clouds Processing Using Nonlocal Neural Networks With Adaptive Sampling. In *Computer Vision and Pattern Recognition (CVPR)*, 2020. 1, 2
- [37] Guandao Yang, Xun Huang, Zekun Hao, Ming Yu Liu, Serge Be-

longie, and Bharath Hariharan. Pointflow: 3D point cloud generation with continuous normalizing flows. In *International Conference on Computer Vision (ICCV)*, 2019. 1, 2, 3, 4, 6, 7, 10, 11

- [38] Manzil Zaheer, Satwik Kottur, Siamak Ravanbakhsh, Barnabás Póczos, Ruslan Salakhutdinov, and Alexander J. Smola. Deep sets. In *Advances in Neural Information Processing Systems (NeurIPS)*, 2017. 1, 2
- [39] Maciej Zamorski, Maciej Zięba, Piotr Klukowski, Rafał Nowak, Karol Kurach, Wojciech Stokowiec, and Tomasz Trzcinski. Adversarial autoencoders for compact representations of 3D point clouds. *Computer Vision and Image Understanding (CVIU)*, 193, 2020. 2

APPENDIX

A. Flow-based Generative Model

A flow-based generative model (or a normalizing flow) f is a neural network composed of a sequence of L invertible transformations g_0, \dots, g_{L-1} , that is, $f = g_{L-1} \circ \dots \circ g_0$ [3, 16]. The model f maps a latent variable z to a sample x in the data space (in short, $x = f(z)$) as

$$z = h_0 \xrightarrow[g_0^{-1}]{g_0} h_1 \xrightarrow[g_1^{-1}]{g_1} h_2 \dots \xrightarrow[g_{L-1}^{-1}]{g_{L-1}} h_L = x. \quad (16)$$

Given the map f , the log-likelihood of a sample x is given by the change-of-variables;

$$\begin{aligned} \log p(x) &= \log p(z) - \log \left| \det \frac{\partial f}{\partial z} \right| \\ &= \log p(z) - \sum_{i=0}^{L-1} \log \left| \det \frac{\partial g_i}{\partial h_i} \right| \\ &= \log p(z) + \log \left| \det \frac{\partial f^{-1}}{\partial x} \right| \\ &= \log p(z) + \sum_{i=0}^{L-1} \log \left| \det \frac{\partial g_i^{-1}}{\partial h_{i+1}} \right|, \end{aligned} \quad (17)$$

where $p(z)$ is a prior, and $\log \left| \det \partial g_i / \partial h_i \right|$ is the log-absolute-determinant of the Jacobian matrix $\partial g_i / \partial h_i$. The prior $p(z)$ of the latent variable z is often set to a simple distribution, such as the standard Gaussian distribution.

Since the calculation of the log-determinant is computationally expensive, each map g_i is often given by a neural network of a specially designed architecture. A coupling-based network is composed of two sub-networks, each of which is applied to the other alternatively [3, 16]. Then, each Jacobian matrix is triangular, and its determinant is easily obtained. A coupling-based network has been proven to approximate arbitrary diffeomorphisms [32]. An autoregressive flow generates an element of the output one-by-one using the remaining elements, also leading to triangular Jacobian matrices [18, 25]. Some other architectures have been proposed [12].

In contrast, a continuous normalizing flow, namely FFJORD [7], defines the map f as the integral of an ordinary differential equation (ODE) $dh/dt = g(h, t)$ and allows general architectures, where $z = h(t_0)$ and $x = h(t_1)$. Given either a sample x or a latent variable z , one can obtain the other by solving the initial value problem with an ODE solver (e.g., the Dormand-Prince method) as

$$x = z + \int_{t_0}^{t_1} g(h(\xi), \xi) d\xi, \text{ or } z = x + \int_{t_1}^{t_0} g(h(\xi), \xi) d\xi. \quad (18)$$

The log-likelihood is given by

$$\log p(x) = \log p(z) - \int_{t_0}^{t_1} \text{Tr} \left(\frac{\partial g(h;t)}{\partial h(t)} \right) dt \quad (19)$$

The log-absolute-determinant is obtained using Hutchinson’s trace estimator [10]. The number of function evaluations, and hence the computational cost, are much larger than those of the discrete counterpart.

B. Model Architecture

ChartPointFlow is adaptable to any network architectures. In our experiments in Section VI, we employed the architectures similar to those of PointFlow [21] and SoftFlow [14] as summarized below.

For the feature encoder E , we employed the architecture same as that used in PointFlow [37]. In particular, the former part was implemented as four 1D convolutional layers with 128-128-256-512 channels and a kernel size of 1; this architecture is equivalent to fully-connected layers applied to each point independently. The latter part was composed of a max-pooling over the points followed by three fully-connected layers with 256-128-128 units. Applied to a set of points, the feature encoder E obtains a permutation-invariant joint representation s_X [4]. Each hidden layer was followed by a batch normalization [11] and the ReLU function. Using the reparameterization trick, the output was regarded as the posterior $q_E(s_X|X)$ of the feature vector s_X .

The prior flow G was also the same as that used in PointFlow [37]. It was composed of three concatsquash layers of 256-256-128 units sandwiched by moving batch normalizations, where these layers are implemented in FFIJORD’s release code [7]. A concatsquash layer is expressed by

$$CS(\chi, \xi) = (W_\chi \chi + b_\chi) \sigma(W_\xi \xi + b_\xi) + W_b \xi + b_b, \quad (20)$$

where W_χ , b_χ , W_ξ , b_ξ , W_b , and b_b are trainable parameters, and σ denotes the sigmoid function. χ and ξ denote the input and condition, which were a point x and the time t in the prior flow G . The first two concatsquash layers were followed by tanh functions as the activation function.

The point generator F was the same as that used in SoftFlow [14] except that ours accepts the label y as a condition while SoftFlow accepts the injected noise’s intensity as a condition. It was composed of nine blocks, each of which was composed of an actnorm, an invertible 1x1 convolution [16], and an autoregressive layer [14]. An autoregressive layer was composed of three concatsquash layers with 256 units followed by a tanh function. The input χ is a point x and the condition ξ is the feature vector s_X . Preliminary experiments suggest that the point generator F of PointFlow, which is based on a continuous normalizing flow, potentially improves the performance, and that it requires too much computational cost for our equipment.

The chart predictor C was composed of three concatsquash layers with 256-256- n units, where n is the number of charts. The chart generator K was composed of five fully-connected layers with 256-512-256-128- n units. Each hidden layer was followed by the ReLU function.

C. Additional Results

1) *Additional Metrics:* As mentioned in Section VI-B, Jensen-Shannon divergence (JSD), minimum matching distance (MMD), coverage (COV) have been used as similarity metrics [1, 21, 22, 14, 37]. While they may give good scores to poor models [14, 37], we summarized their results just for reference. JSD measures the distance between two empirical distributions P_1 and P_2 . For JSD, a canonical voxel grid was introduced, the number of points lying in each voxel was counted, and then an empirical probability distribution was obtained for each of the reference set and the generated set. MMD is the distance between a point cloud in the reference set and its nearest neighbor in the generated set. COV measures the fraction of point clouds in the reference set that can be matched at least one in the generated set. We summarized the results in Table A1. ChartPointFlow achieved the best scores in many cases.

2) *The Number of Charts:* We also provide the results of the generation and reconstruction tasks with the varying number of charts in Tables A2 and A3. A larger number n of charts tends to lead to a better score. Recall that the computational cost of the proposed method is constant independently of the number n of charts, thanks to the Gumbel-Softmax approach [13].

3) *Additional Images:* We also provide additional results for the qualitative assessment.

Figure A1 summarizes samples generated by ChartPointFlow. One can see that a wide variety of objects are generated, and the same chart is assigned to the same subpart across objects, such as the airplane wings, chair legs, and car wheels.

Figure A2 shows the point clouds obtained by the linear interpolation of the feature vector s_X between two point clouds. For improving the visibility, we set the number n of charts to 8. In the case of the airplane category, each set of a wing and an engine has its own chart at the leftmost column (see the green and red points). Following the change in the feature vector s_X , the engines disappear and the wings move upward with the same charts. This result implies that charts are assigned to the semantic subparts and not to the absolute positions. The same goes for the car wheels. At the leftmost column in the chair category, each of the four legs is covered by its own chart. With the changing feature vector s_X , the two legs on each side come close to each other and collide, forming a different structure. In this way, ChartPointFlow expresses a variety of shapes by a continuous deformation.

Figures A3, A4, and A5 summarize the reconstruction results of objects used for training (i.e., seen objects). Due to the randomness of the point generator F , the reconstruction results are not completely the same as the original point clouds. This problem setting can evaluate the performance on the super-resolution task. Only ChartPointFlow preserves the holes in the chairs’ backrests and armrests clearly.

Figures A6, A7, and A8 summarize the reconstruction results of objects unused for training (i.e., unseen objects). ChartPointFlow reconstructs the chair in the leftmost column

Category	Model	JSD(\downarrow)	MMD(\downarrow)		COV($\%$, \uparrow)		1-NNA($\%$)	
			CD	EMD	CD	EMD	CD	EMD
Airplane	r-GAN [1]	7.44	0.261	5.47	42.72	18.02	93.58	99.51
	l-GAN (CD) [1]	4.62	0.239	4.27	43.21	21.23	86.30	97.28
	l-GAN (EMD) [1]	3.61	0.269	3.29	47.90	50.62	87.65	85.68
	PC-GAN [21]	4.63	0.287	3.57	36.46	40.94	94.35	92.32
	PointFlow [37]	4.92	0.217	3.24	46.91	46.91	75.68	75.06
	SoftFlow [14]	-	-	-	-	-	70.92	69.44
	ChartPointFlow (proposed)	3.01	0.214	3.06	50.20	51.79	69.39	65.62
Chair	r-GAN [1]	11.5	2.57	12.8	33.99	9.97	71.75	99.47
	l-GAN (CD) [1]	4.59	2.46	8.91	41.39	25.68	64.43	85.27
	l-GAN (EMD) [1]	2.27	2.61	7.85	40.79	41.69	64.73	65.56
	PC-GAN [21]	3.90	2.75	8.20	36.50	38.98	76.03	78.37
	PointFlow [37]	1.74	2.24	7.87	46.83	46.98	60.88	59.89
	SoftFlow [14]	-	-	-	-	-	59.95	63.51
	ChartPointFlow (proposed)	1.83	2.52	7.84	45.61	45.85	57.89	58.31
Car	r-GAN [1]	12.8	1.27	8.74	15.06	9.38	97.87	99.86
	l-GAN (CD) [1]	4.43	1.55	6.25	38.64	18.47	63.07	88.07
	l-GAN (EMD) [1]	2.21	1.48	5.43	39.20	39.77	69.74	68.32
	PC-GAN [21]	5.85	1.12	5.83	23.56	30.29	92.19	90.87
	PointFlow [37]	0.87	0.91	5.22	44.03	46.59	60.65	62.36
	SoftFlow [14]	-	-	-	-	-	62.63	64.71
	ChartPointFlow (proposed)	0.86	0.91	5.13	46.41	48.81	58.13	58.80

TABLE A1: Generation performances. The scores are multiplied by 10^2 for JSD and MMD-EMD, and by 10^3 for MMD-CD. \uparrow denotes that a higher score is better. \downarrow denotes that a lower score is better.

well, while others deform the round backrest in a rectangular shape. Due to the limitation of flexibility, existing methods have a difficulty even in reconstruction.

Category	Number of Chart	JSD(\downarrow)	MMD(\downarrow)		COV(%, \uparrow)		1-NNA(%)	
			CD	EMD	CD	EMD	CD	EMD
Airplane	1	3.54	0.221	3.15	49.63	53.21	72.67	68.90
	4	3.62	0.220	3.11	48.89	51.79	71.77	67.30
	8	3.39	0.217	3.08	49.66	51.70	70.90	66.54
	12	3.60	0.213	3.06	48.40	51.73	70.20	65.99
	16	3.93	0.215	3.07	49.52	51.08	70.72	66.48
	20	3.82	0.218	3.09	48.10	51.02	71.20	66.53
	24	3.01	0.214	3.06	50.20	51.79	69.39	65.62
Chair	1	1.96	2.50	8.06	43.04	45.38	59.75	63.16
	4	1.96	2.48	7.90	43.45	44.30	59.64	61.79
	8	1.82	2.50	7.86	43.85	44.76	58.76	60.44
	12	1.89	2.54	7.87	44.82	45.50	58.37	59.96
	16	1.57	2.48	7.78	45.37	46.03	58.04	59.51
	20	1.83	2.52	7.84	45.61	45.85	57.89	58.31
	24	1.97	2.53	7.87	45.05	45.69	58.20	59.29
Car	1	0.96	0.95	5.25	44.98	47.78	61.86	61.56
	4	0.93	0.92	5.17	46.20	46.86	60.94	60.48
	8	0.91	0.90	5.15	45.42	46.45	60.04	60.84
	12	0.93	0.92	5.14	44.76	46.31	59.50	59.76
	16	0.86	0.91	5.13	46.41	48.81	58.13	58.80
	20	0.83	0.92	5.14	45.38	46.89	59.10	59.65
	24	0.87	0.94	5.14	44.83	47.66	59.42	58.68

TABLE A2: Generation performances with different numbers of charts. The scores are multiplied by 10^2 for JSD and MMD-EMD, and by 10^3 for MMD-CD. \uparrow denotes that a higher score is better. \downarrow denotes that a lower score is better.

Category	Number of Chart	CD	EMD
Airplane	1	1.18	2.64
	4	1.13	2.40
	8	1.13	2.32
	12	1.14	2.30
	16	1.09	2.26
	20	1.08	2.25
	24	1.07	2.23
Chair	1	11.76	6.92
	4	10.89	5.82
	8	10.43	5.47
	12	9.40	4.90
	16	9.04	4.71
	20	8.76	4.64
	24	8.78	4.62
Car	1	6.95	5.47
	4	6.78	4.58
	8	6.66	4.39
	12	6.56	4.19
	16	6.34	4.12
	20	6.31	4.08
	24	6.20	3.96

TABLE A3: Reconstruct performance evaluated by CD ($\times 10^4$) and EMD ($\times 10^2$).

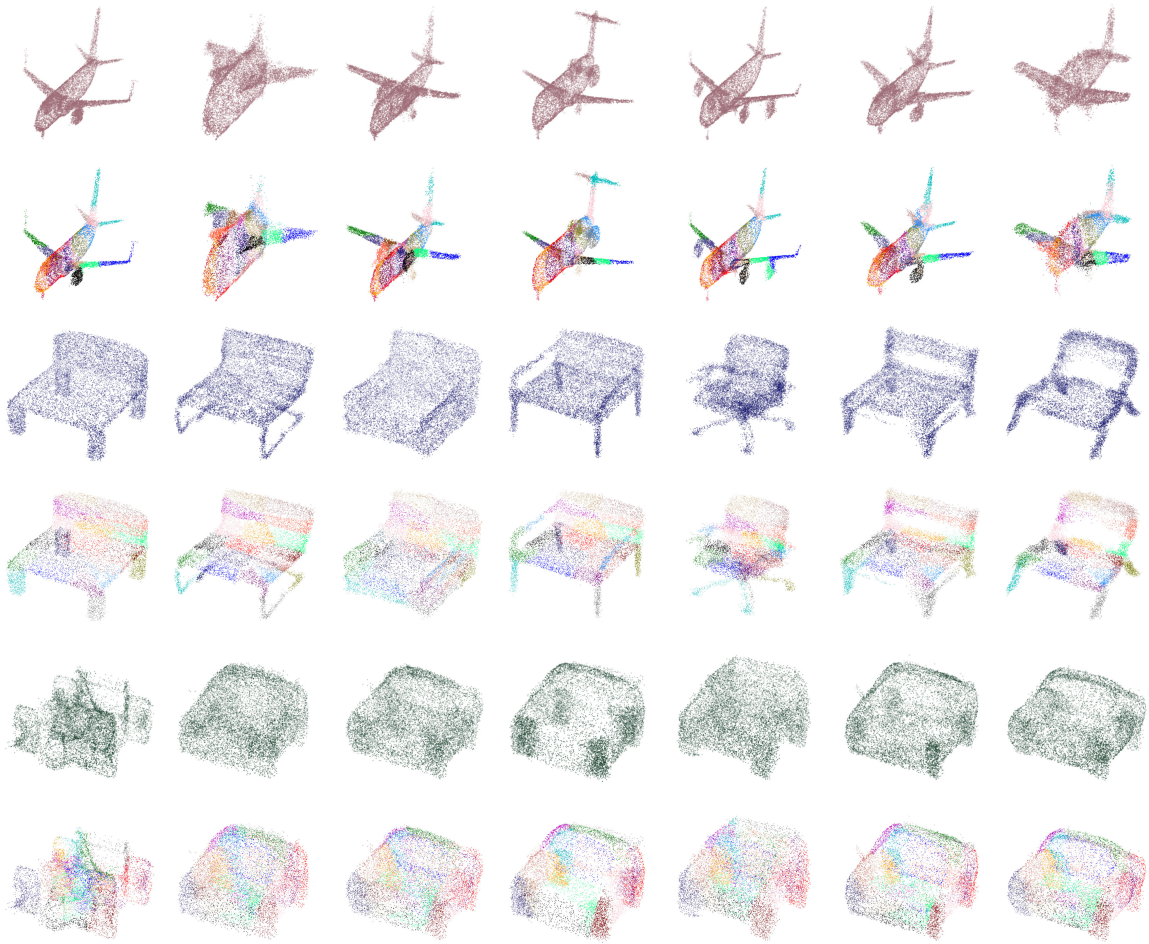


Fig. A1: Generation examples by ChartPointFlow.

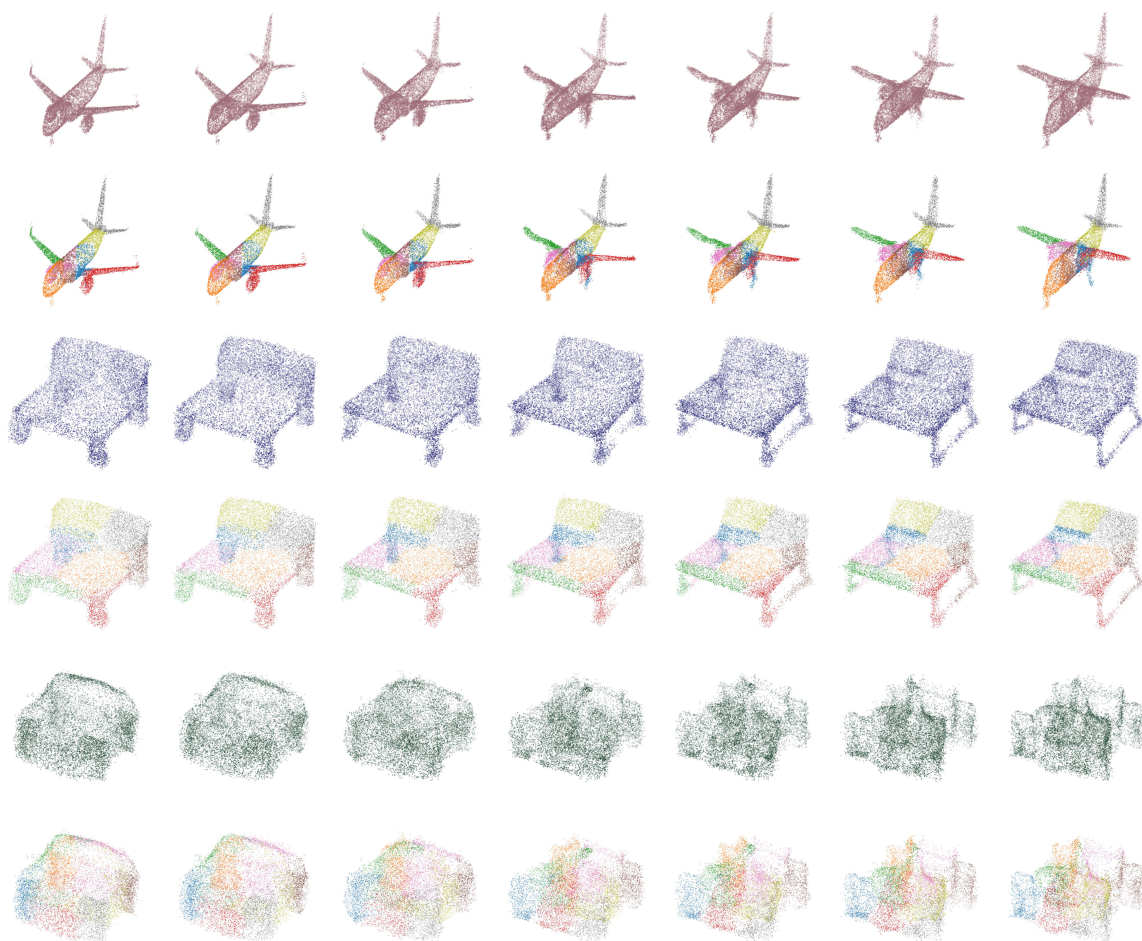


Fig. A2: Linear interpolation of the feature vector s_X between two point clouds.

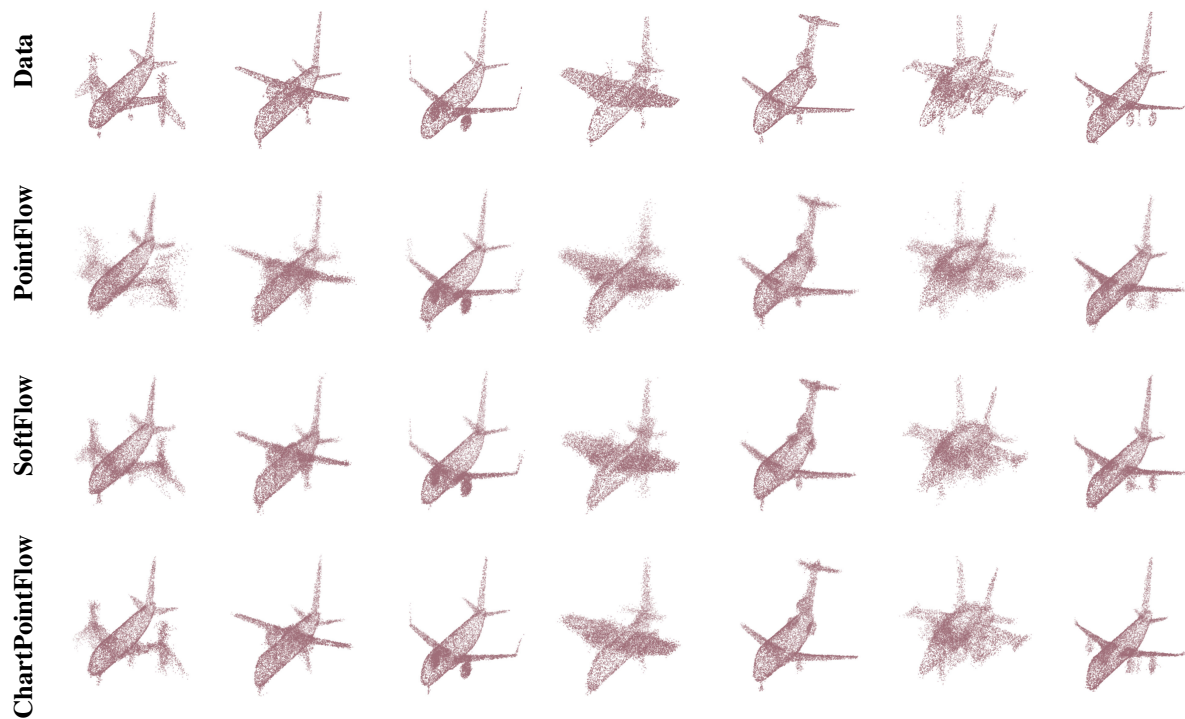


Fig. A3: Reconstruction examples of seen airplanes (i.e., super-resolution).

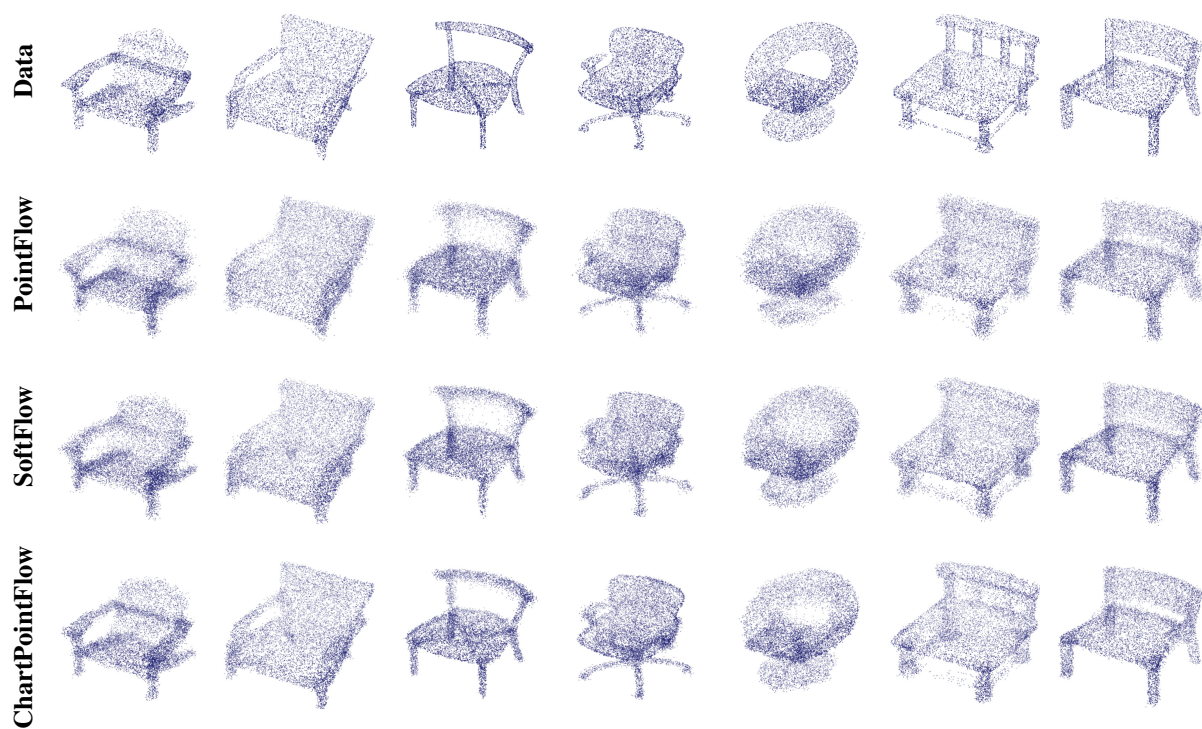


Fig. A4: Reconstruction examples of seen chairs (i.e., super-resolution).

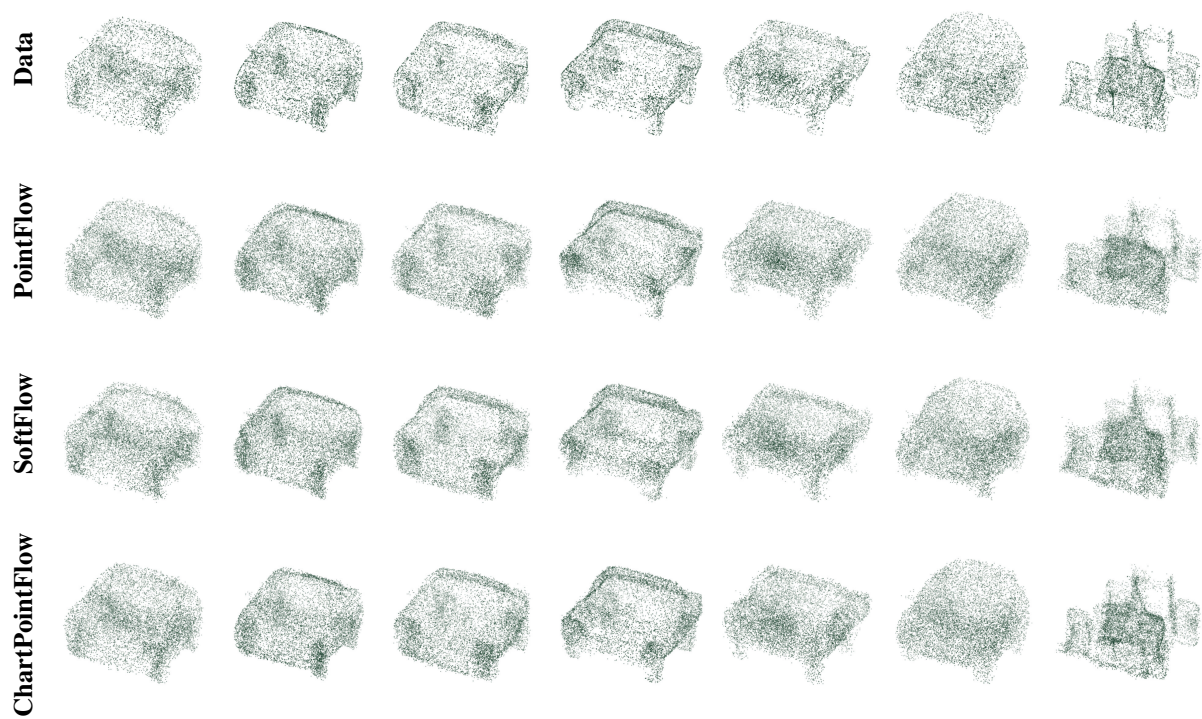


Fig. A5: Reconstruction examples of seen cars (i.e., super-resolution).

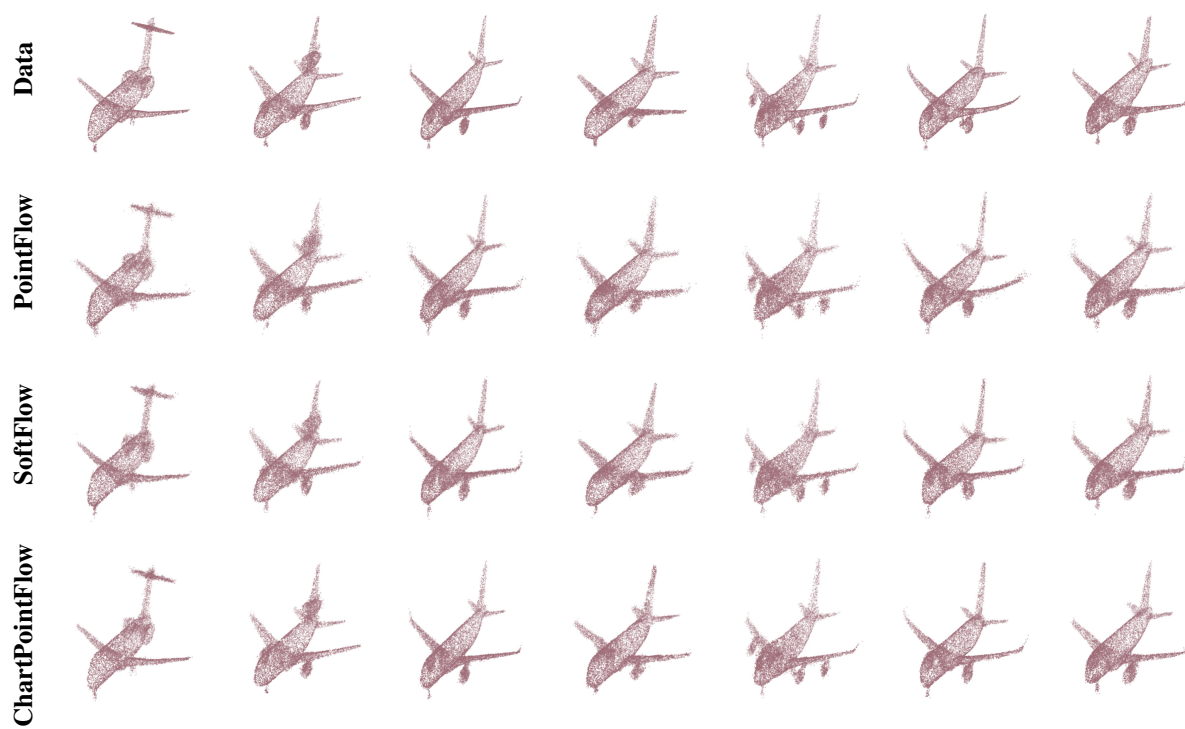


Fig. A6: Reconstruction examples of unseen airplanes.

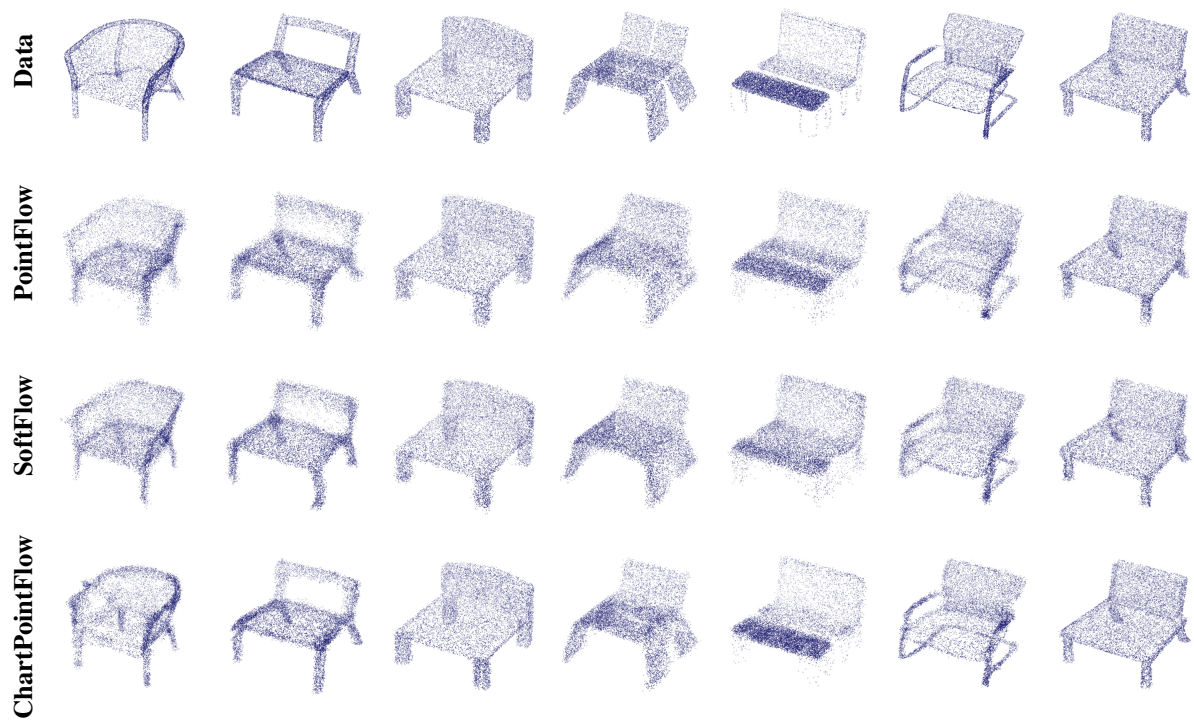


Fig. A7: Reconstruction examples of unseen chairs.

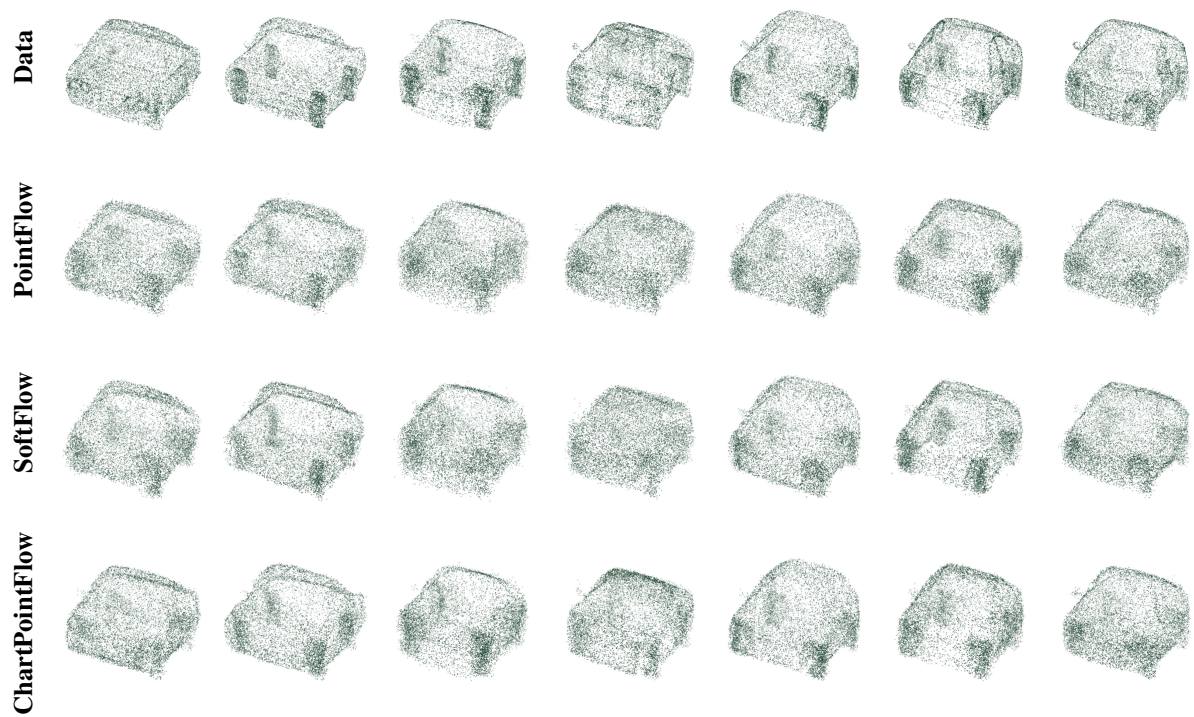


Fig. A8: Reconstruction examples of unseen cars.